J. Fluid Mech. (2024), *vol*. 995, R3, doi:10.1017/jfm.2024.611

Linear stability analysis of generalized Couette–Poiseuille flow: the neutral surface and critical properties

W. Cheng[1], **H. Ma**[1], **D.I. Pullin**[2] **and X. Luo**[1],†

[1]School of Engineering Science, University of Science and Technology of China, Hefei 230026, PR China

[2]Graduate Aerospace Laboratories, California Institute of Technology, CA 91125, USA

(Received 27 March 2024; revised 9 May 2024; accepted 3 June 2024)

We discuss the modal, linear stability analysis of generalized Couette–Poiseuille (GCP) flow between two parallel plates moving with relative speed in the presence of an applied pressure gradient vector inclined at an angle $0 \leqslant \phi \leqslant 90^\circ$ to the plate relative velocity vector. All possible GCP flows can be described by a global Reynolds number Re, ϕ and an angle $0 \leqslant \theta \leqslant 90^\circ$, where $\cos\theta$ is a measure of the relative weighting of Couette flow to the composite GCP flow. This provides a novel and uncommon group of generally three-dimensional base velocity fields with wall-normal twist, for which Squire's theorem does not generally apply, requiring study of oblique perturbations with wavenumbers (α, β). With (θ, ϕ) fixed, the neutral surface $f(\theta, \phi; Re, \alpha, \beta) = 0$ in (Re, α, β) space is discussed. A mapping from GCP to plane Couette–Poiseuille flow stability is found that suggests a scaling relation $Re^*\alpha/k = H(\theta^*)$ that collapses all critical parameters, where $Re^* = Re\,(\alpha_1/\alpha)\,(\sin\theta/\sin\theta^*)$ and $\tan\theta^* = (\alpha_1/\alpha)\tan\theta$, with $\alpha_1 = \alpha\cos\phi + \beta\sin\phi$. This analysis does not, however, directly reveal global critical properties for GCP flow. The global $Re_{cr}(\theta, \phi)$ shows continuous variation, while $\alpha_{cr}(\theta, \phi)$ and $\beta_{cr}(\theta, \phi)$ show complex behaviour, including discontinuities owing to jumping of critical states across neighbouring local valleys (in Re) or lobes of the neutral surface. The discontinuity behaviour exists for all low ϕ. For $\phi \gtrsim 21^\circ$, variations of $\alpha_{cr}(\theta)$ and $\beta_{cr}(\theta)$ are generally smooth and monotonic.

Key words: shear-flow instability

1. Introduction

Flows between two parallel plates are canonical configurations involving abundant flow stability and turbulence phenomena. Stability analyses of plane Poiseuille (PP) flow

† Email address for correspondence: xluo@ustc.edu.cn

driven by an external pressure gradient, and plane Couette (PC) flow induced by bounding, moving walls, are classical examples. For PP flow, asymptotic solutions of the Orr–Sommerfeld equation (Lin 1945) provided a critical Reynolds number $Re_{cr} \approx 5300$ for modal flow instability, with a more accurate $Re_{cr} = 5772.22$ given later by Orszag (1971). Evidence for linear stability of PC flow was shown by Gallagher & Mercer (1962) and Deardorff (1963). Later, Romanov (1973) proved that, for modal perturbations, if the perturbation wavenumber is $\alpha > 0$ and Reynolds number is $Re > 0$, then the flow is linearly stable.

Subsequent research has focused on extensions such as plane Couette–Poiseuille (PCP) flow, where the plate relative velocity vector and the externally applied pressure gradient are aligned. Stability of PCP was studied by Potter (1966) and Hains (1967), offering numerical evidence for the consensus view that a Couette component stabilizes the flow. Later, Cowley & Smith (1985) studied the asymptotic behaviour of neutral curves for PCP flow at large Reynolds numbers, modifying the earlier results of Smith (1979) for PP flow. More recently, Kirthy & Diwan (2021) conducted an energy budget analysis, pointing out that upper plate movement causes a negative production term, thus leading to stabilization. Guha & Frigaard (2010) and Shankar & Shivakumara (2021) investigated PCP stability, emphasizing certain volume flow aspects that correspond to a mechanical alternative for stabilization. Stability of PCP flow for other fluid constitutive relationships has been studied, including non-Newtonian (Nouar *et al.* 2007; Sengupta & De 2020; Pal & Samanta 2023) and non-ideal (Ren, Fu & Pecnik 2019) fluids. Related work focusing on Couette–Poiseuille flow between concentric cylinders was reported by Sadeghi & Higgins (1991) and Gittler (1993) for both inner and outer stationary cylinder motions, respectively. Non-modal operator based methods have been applied to PP, PC and PCP flows (Böberg & Brösa 1988; Butler & Farrell 1992; Reddy & Henningson 1993; Bergström 2005; Schmid 2007), providing a novel perspective on transient growth in the early stages of turbulence transition.

A generalized Couette–Poiseuille (GCP) flow was defined by Cheng *et al.* (2023) as a channel-like, wall-bounded flow with non-parallel superposition of a PP and a PC flow, thus forming a three-dimensional (3-D) base flow velocity profile as a further extension of PCP flow. Squire's theorem (Squire 1933) for PCP flow allows determination of a critical Reynolds number for general perturbations to the plane-parallel base flow by restriction to planar or two-dimensional disturbances. For GCP flow, Squire's theorem cannot be applied directly. In § 2, the GCP flow configuration is defined in terms of superposed base flows, and the relevant stability equation is obtained. Numerical determination of neutral surfaces is described in § 3, and global and local critical points are defined. A mapping from GCP stability to an equivalent PCP stability problem is also identified that allows reduction in the dimensionality of local critical point dependence on the flow parameters. Global GCP stability properties are explored in § 4, which reveals complex behaviour in the dependence of the critical Reynolds number and corresponding wavenumbers as functions of (θ, ϕ). Conclusions and future perspectives are discussed in § 5.

2. Problem description: GCP flow

In Cartesian coordinates $(\hat{x}, \hat{y}, \hat{z})$ ('hat' denoting dimensional) and velocity components $(\hat{U}, \hat{V}, \hat{W})$, the top and bottom walls at $\hat{y} = \pm h$ move in the $\pm\hat{x}$-directions with $\hat{x}$ velocity components $\hat{U}_C$ and $-\hat{U}_C$, respectively. The base flow is an exact solution of the steady Navier–Stokes equations for an incompressible fluid of constant density and viscosity

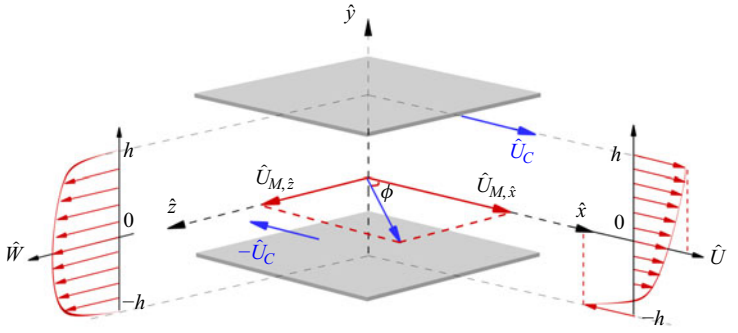

Figure 1. Configuration of GCP flow with distance $2h$ between two walls moving with $\hat{x}$ velocities $\pm\hat{U}_C$. The angle ϕ describes the inclination of the bulk velocity vector to the $\hat{x}$-axis.

ρ, μ, respectively, with $(\hat{U}, \hat{V}, \hat{W}) = (\hat{U}(\hat{y}), 0, \hat{W}(\hat{y}))$ in the presence of constant, given, mean pressure gradients in both the $\hat{x}$- and $\hat{z}$-directions, and with boundary conditions $(\hat{U}, \hat{V}, \hat{W}) = (-\hat{U}_C, 0, 0)$ at $\hat{y} = -h$, and $(\hat{U}, \hat{V}, \hat{W}) = (\hat{U}_C, 0, 0)$ at $\hat{y} = h$. Instead of pressure gradients, we work with bulk mass flow speeds $\hat{U}_{M,\hat{x}} = \int_{-h}^{h} \hat{U}(\hat{y})\,\mathrm{d}\hat{y}/2h$ and $\hat{U}_{M,\hat{z}} = \int_{-h}^{h} \hat{W}(\hat{y})\,\mathrm{d}\hat{y}/2h$. The base flow can then be expressed as

$$(\hat{U}, \hat{V}, \hat{W}) = \left(-\frac{3}{2}\,\hat{U}_{M,\hat{x}}\left(\left(\frac{\hat{y}}{h}\right)^2 - 1\right) + \hat{U}_C\left(\frac{\hat{y}}{h}\right), 0, -\frac{3}{2}\,\hat{U}_{M,\hat{z}}\left(\left(\frac{\hat{y}}{h}\right)^2 - 1\right)\right). \quad (2.1)$$

This is a linear combination of Couette flow in the $\hat{x}$–$\hat{y}$ plane and PP flows in both the $\hat{x}$- and $\hat{z}$-directions. For the present linear base flow, the vector formed by the two bulk flow speeds as components is parallel to the pressure gradient vector. Both form an angle ϕ to the $\hat{x}$-axis, as shown in figure 1.

The parameters $(\hat{U}_C, \hat{U}_{M,\hat{x}}, \hat{U}_{M,\hat{z}})$ are independent speed variables of the GCP flow. Three independent Reynolds numbers based on these speeds form the all-positive octant of a 3-D Cartesian space. It is convenient instead to work in a spherical coordinate system in this space, with variables (Re, θ, ϕ) defined as

$$Re = \frac{\rho\hat{U}_0 h}{\mu}, \quad \theta = \arccos\left(\frac{\hat{U}_C}{\hat{U}_0}\right), \theta \in [0^\circ, 90^\circ], \quad \phi = \arctan\left(\frac{\hat{U}_{M,\hat{z}}}{\hat{U}_{M,\hat{x}}}\right), \phi \in [0^\circ, 90^\circ], \quad (2.2a\text{–}c)$$

where $\hat{U}_0 = (\hat{U}_C^2 + \hat{U}_{M,\hat{x}}{}^2 + \hat{U}_{M,\hat{z}}{}^2)^{1/2}$ is a global velocity scale, μ is the dynamic viscosity, $\cos\theta$ is a measure of the relative weighting of Couette-type flow and composite base flow, and ϕ is the angle between the moving plates velocity vector and the bulk velocity vector. The angle ϕ can also be interpreted as a measure of the bulk velocity ratio in two wall-parallel directions. Dimensionless base flow velocities scaled on $\hat{U}_0$ are given by

$$U = \frac{\hat{U}}{\hat{U}_0} = -\frac{3}{2}\cos\phi\sin\theta\,(y^2 - 1) + y\cos\theta, \quad W = \frac{\hat{W}}{\hat{U}_0} = -\frac{3}{2}\sin\phi\sin\theta\,(y^2 - 1), \quad (2.3a,b)$$

with $y = \hat{y}/h$. This comprises the non-parallel, 3-D GCP base flow $\boldsymbol{U}(y) = (U(y), 0, W(y))$, as illustrated in figure 1 in dimensional coordinates.

When $\theta \to 0^\circ$, the flow approaches pure PC flow for all ϕ. When $\theta \to 90^\circ$, it approaches pure PP flow at an angle ϕ to the x-axis. When $\phi \to 0^\circ$, the directions of Couette flow and Poiseuille flow coincide. This is PCP flow. When $\phi \to 90^\circ$, Couette and Poiseuille flow are orthogonal. The base flow velocity vector always lies in an x–z plane. For PCP flow, the velocity vector also lies in the x–y plane, which we refer to as a 'parallel' base flow. For $\phi > 0^\circ$, the velocity vector is generally at a finite angle (which is a function of y) to the x-axis, except at $y = 1, -1$, where the velocity vector makes angles 0° and 180°, respectively, with the positive x-axis. We call this 'non-parallel' flow.

2.1. *Stability equations*

An infinitesimal linear perturbation $(\epsilon\tilde{\boldsymbol{u}}, \epsilon\tilde{p})$ with $\epsilon \ll 1$ is imposed on the base flow $(\boldsymbol{U}, P)$, with P the base pressure distribution. The perturbed flow is given by

$$(\boldsymbol{U} + \epsilon\tilde{\boldsymbol{u}}, P + \epsilon\tilde{p}) = (U + \epsilon\tilde{u}, \epsilon\tilde{v}, W + \epsilon\tilde{w}, P + \epsilon\tilde{p}). \tag{2.4}$$

The disturbance quantities $(\tilde{\boldsymbol{u}}, \tilde{p})$ are spatially periodic and have the form

$$(\tilde{u}, \tilde{v}, \tilde{w}, \tilde{p}) = (u(y), v(y), w(y), p(y)) \exp(\mathrm{i}(\alpha x + \beta z - \Omega t)), \tag{2.5}$$

where $\Omega \in \mathbb{C}$ is the complex frequency, $\alpha, \beta \in \mathbb{R}$ are the x- and z-direction wavenumbers, respectively, and $u(y)$, $v(y)$, $w(y)$ and $p(y)$ represent perturbation amplitudes. Putting $\alpha = k\cos\chi$, $\beta = k\sin\chi$, the perturbation can be interpreted as a wave form in the x–z plane with wavenumber vector oriented at an angle χ to the x-axis.

The linear modal stability equations are obtained by using the base flow perturbed by (2.5) in the incompressible flow continuity and Navier–Stokes equations, expanding in ϵ, and truncating at first order, $O(\epsilon)$. This gives

$$\left.\begin{aligned} \mathrm{i}(\alpha u + \beta w) + Dv &= 0, \\ -\mathrm{i}\Omega u + (\mathrm{i}\alpha U + \mathrm{i}\beta W)u + v \times DU + \mathrm{i}\alpha p &= \frac{1}{Re}(D^2 - k^2)u, \\ -\mathrm{i}\Omega v + (\mathrm{i}\alpha U + \mathrm{i}\beta W)v + Dp &= \frac{1}{Re}(D^2 - k^2)v, \\ -\mathrm{i}\Omega w + (\mathrm{i}\alpha U + \mathrm{i}\beta W)w + v \times DW + \mathrm{i}\beta p &= \frac{1}{Re}(D^2 - k^2)w, \end{aligned}\right\} \tag{2.6}$$

where $k = (\alpha^2 + \beta^2)^{1/2}$ is a resultant wavenumber, and $D \equiv \mathrm{d}/\mathrm{d}y$. Since there are three independent spatial variables (x, y, z), a stream function for the perturbed flow, which is typically used in PCP stability analysis, does not appear to exist. After some algebra, a modified Orr–Sommerfeld (OS) stability equation is given as

$$\left[(U_P - c) + \frac{\alpha}{\alpha_1} y\cos\theta\right](D^2 - k^2)v - v \times D^2 U_P = \frac{1}{\mathrm{i}\alpha_1 Re}(D^2 - k^2)^2 v, \tag{2.7}$$

with

$$U_P(y, \theta) = -\tfrac{3}{2}(y^2 - 1)\sin\theta, \quad \alpha_1 = \alpha\cos\phi + \beta\sin\phi. \tag{2.8a,b}$$

Here, U_P is a characteristic velocity profile denoting the Poiseuille component driven by the bulk mass flow, which gives $U = U_P\cos\phi + y\cos\theta$ and $W = U_P\sin\phi$. An orientational wavenumber α_1 is introduced, with geometric angle ϕ involved. This also

suggests perturbation rearrangement by defining the complex phase velocity $c = \Omega/\alpha_1$ ($c = c_r + \mathrm{i}c_i$). We note that α_1 differs from the resultant wavenumber vector k.

For completeness, a corresponding modified Squire equation is also derived. With the definition $\eta = \partial u/\partial z - \partial w/\partial x$, the linearized y-direction vorticity equation gives

$$-\mathrm{i}\Omega\eta + (\mathrm{i}\alpha U + \mathrm{i}\beta W)\eta = \mathrm{i}(\alpha \times DW - \beta \times DU)v + \frac{1}{Re}(D^2 - k^2)\eta. \tag{2.9}$$

Referring to (2.8*a*,*b*), a modified Squire equation is derived as

$$\left[(U_P - c) + \frac{\alpha}{\alpha_1} y\cos\theta\right]\eta - \frac{1}{\mathrm{i}\alpha_1 Re}(D^2 - k^2)\eta = \left[\frac{1}{\alpha_1}(\alpha\sin\phi - \beta\cos\phi)\,DU_P - \frac{\beta}{\alpha_1}\cos\theta\right]v. \tag{2.10}$$

Boundary conditions for the modified OS and Squire equations are $v(\pm1) = \eta(\pm1) = 0$ and $Dv(\pm1) = 0$. In stability analysis, we focus on the sign of the imaginary part of the least stable mode, $c_{i,max}$. For Squire modes, it can be shown that

$$c_{i,Squire}\int_{-1}^{1}|\eta|^2\,\mathrm{d}y = -\frac{1}{\alpha_1 Re}\int_{-1}^{1}|D\eta|^2 + k^2|\eta|^2\,\mathrm{d}y < 0. \tag{2.11}$$

The Squire modes are thus always damped, leading the disturbances to attenuate consistently.

The OS equation (2.7) with boundary conditions produces a generalized eigenvalue problem with five parameters: θ, ϕ, Re, α and β. Then for fixed θ and ϕ, an isosurface $c_i = 0$ can be determined in (Re, α, β) space. This is referred to as the neutral surface.

2.2. *Numerical method*

A spectral collocation method is adopted where the coefficient matrices are constructed in a Chebyshev domain using $v(y) = \sum_{n=0}^{N} a_n T_n(y)$ and $y_j = \cos(j\pi/N)$, where a_n is the coefficient of the nth Chebyshev polynomial $T_n(y)$, truncated at order N. Thus the generalized eigenvalue problem can be stated as $\boldsymbol{A}\,\boldsymbol{a} = c\boldsymbol{B}\,\boldsymbol{a}$, with $\boldsymbol{A}$ and $\boldsymbol{B}$ the coefficient matrices, and $\boldsymbol{a}$ the eigenvectors. The calculation is done using the QZ algorithm. The numbers of collocation points are chosen to guarantee that the maximum relative error of c_i, the imaginary part of the eigenvalues, for the five least stable modes is below 10^{-5}, specifically at high Reynolds number and small wavenumbers.

Numerical verification is implemented with literature data on PCP flow stability with three parameters $(\theta; Re, \alpha)$. Neutral curves in $(\theta; Re, \alpha)$ space are shown in figure 2(*a*). Three cuts at constant $\theta = 90°$, 81.5° and 73.3° are also shown. The locus of minimum or critical Reynolds number $Re_{cr}(\theta)$ is shown using red triangles. The corresponding critical wavenumber is $\alpha_{cr}(\theta)$. Three neutral curves at fixed θ are plotted in the Re–α plane in figure 2(*b*). The present neutral curves for $\theta = 90°$, 81.5° and 73.3° agree well with data by Potter (1966), which are marked as symbols.

3. Global and local critical states

With (θ, ϕ) fixed, we calculate $c_i(Re, \alpha, \beta)$, from which the neutral surface $f(\theta, \phi; Re, \alpha, \beta) = 0$ corresponding to the isosurface $c_i = 0$ can be determined. The scheme for this is discussed below. Global critical parameters are the minimum $Re_{cr} = Re$

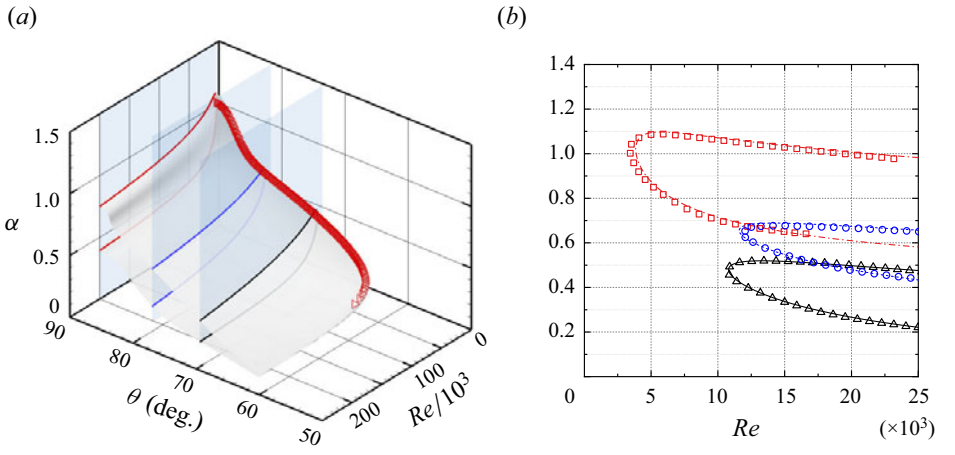

Figure 2. The PCP ($\phi = 0^\circ$) stability. (*a*) Neutral curves in (θ; Re, α) space. Coloured lines are neutral curves defined as surface cuts by planes of constant θ. Red triangles indicate the trajectory of local critical points with (Re_{cr}, α_{cr}) at each θ. (*b*) Comparison of three extracted neutral curves at different θ: 90° (red dot-dashed line), 81.5° (blue dashed line) and 73.3° (black solid line). Lines indicate present results, and symbols indicate data from Potter (1966).

on this surface with corresponding α_{cr}, β_{cr}, and with stability for $Re < Re_{cr}$. An example is shown in figure 3(*a*) with $\phi = 45^\circ$, $\theta = 80^\circ$ where the critical state is marked with a red dot. If we fix $\chi > 0^\circ$, then this defines a plane in (Re, α, β) space, $\alpha = \beta \cot \chi$. We can then define a local critical state as the minimal $Re_{cr,l} = Re$, together with corresponding wavenumbers ($\beta_{cr,l} \cot \chi$, $\beta_{cr,l}$) on the planar curve defined by the intersection of this plane with the neutral surface as defined above. A local critical state thus represents neutral stability of a GCP flow for a perturbation with specified direction χ. One example of a local critical point with $\chi = \pi/4$, marked as a square, is shown in black in figure 3(*a*).

3.1. *Mapping from GCP to PCP flow stability*

Equation (2.7) can be reduced to a 3-D perturbed PCP OS equation ($\phi = 0^\circ$), given by

$$\left[(U_P - c) + y\cos\theta\right](D^2 - k^2)v - v \times D^2 U_P = \frac{1}{\mathrm{i}\alpha\, Re}(D^2 - k^2)^2 v, \tag{3.1}$$

where we still have $k = (\alpha^2 + \beta^2)^{1/2}$, and now $\alpha_1 = \alpha$. This represents a PCP stability equation, but Squire's theorem, where one puts $\beta = 0$, $k = \alpha$, has not been utilized.

To draw an analogy to the PCP equation (3.1), multiplying the modified OS equation (2.7) by $\sin\theta^*/\sin\theta$, we can obtain

$$\left[(U^* - c^*) + y\cos\theta^*\right](D^2 - k^2)v - v \times D^2 U^* = \frac{1}{\mathrm{i}\alpha\, Re^*}(D^2 - k^2)^2 v, \tag{3.2}$$

where $*$ denotes mapping parameters defined as

$$\tan\theta^* = \frac{\alpha_1}{\alpha}\tan\theta, \quad c^* = c\frac{\sin\theta^*}{\sin\theta}, \quad U^* = -\frac{3}{2}(y^2 - 1)\sin\theta^*, \quad Re^* = Re\,\frac{\alpha_1}{\alpha}\frac{\sin\theta}{\sin\theta^*}. \tag{3.3a–d}$$

Comparing (3.1) to (3.2) shows that the latter can be interpreted as the OS equation for an equivalent PCP flow with $\theta \to \theta^*$ and $Re \to Re^*$. Hence the full GCP stability equation can be mapped to that for a defined PCP stability.

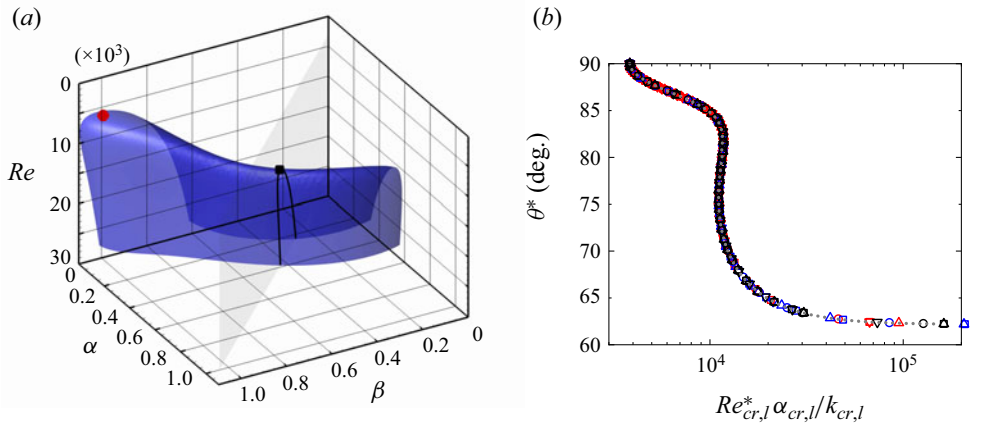

Figure 3. The GCP stability illustration. (*a*) Example of a neutral surface in (α, β, Re) space at fixed $\phi = 45^\circ$ and $\theta = 80^\circ$. The red dot indicates the global critical point with $(\alpha_{cr}, \beta_{cr}, Re_{cr}) = (0.041, 1.016, 5414.88)$. The intersection between a plane surface $\alpha = \beta \cot\chi$ with $\chi = \pi/4$ and the neutral surface generates a local neutral curve (black) and a corresponding local critical point (black square) $(\alpha_{cr,l}, Re_{cr,l}) = (0.489, 11674.89)$. (*b*) Mapping local critical Reynolds number $Re^*_{cr,l}$ in plot of θ^* versus $Re^*_{cr,l}\alpha_{cr,l}/k_{cr,l}$. Values of $\cot\chi$: red, 0.1; black, 1; blue, 10. Values of ϕ: square, 30°; circle, 45°; up triangle, 60°; down triangle, 90°. The dotted line indicates PCP results.

For (3.2), for given θ^*, a neutral surface $f^*(\theta^*; Re^*, \alpha, \beta) = 0$ can be determined. The equivalent PCP critical state (Re^*_{cr}, α_{cr}) will be at the Re^* minimum of the curve formed by the intersection of this surface with the plane $\beta = 0$. This is irrelevant to the GCP stability problem because Squire's theorem does not apply. So for given (θ, ϕ), the global GCP critical point $(Re_{cr}, \alpha_{cr}, \beta_{cr})$ will map onto a point on the neutral surface $f^* = 0$, but this will not generally coincide with the equivalent PCP critical state.

The above mapping admits definition of a local critical Reynolds number $Re^*_{cr,l}$, which is the mapped value of $Re_{cr,l}$. In other words, $Re^*_{cr,l}$ is the minimum Re^* on the intersection of the plane $\alpha = \beta\cot\chi$ with the neutral surface $f^*(\theta^*; Re^*, \alpha, \beta) = 0$. So for given θ^*, it is the minimum Re^* on the curve in the Re^*–β plane $f^*(\theta^*; Re^*, \beta\cot\chi, \beta) = 0$. This states that $Re^*_{cr,l} = G(\theta^*, \chi)$, where G is some function to be determined numerically. This can be simplified by writing $1/(\mathrm{i}\alpha\, Re^*)$ on the right-hand side of (3.2) as $1/(\mathrm{i}k\,\widetilde{Re})$, where $\widetilde{Re} = Re^*\cos\chi$ (recall that $\cos\chi = \alpha/k$). If χ is fixed, corresponding to a local critical state, then (3.2) contains parameters $(\theta^*; \widetilde{Re}, k)$ only. It follows that the local critical Reynolds number must be of the form $\widetilde{Re}_{cr,l} = H(\theta^*)$, or equivalently $Re^*_{cr,l}\alpha_{cr,l}/k_{cr,l} = H(\theta^*)$.

In figure 3(*b*), calculated values of $Re^*_{cr,l}\alpha_{cr,l}/k_{cr,l}$ collapse well versus θ^*. The dotted line represents data obtained directly for PCP flow using (3.2). The symbols represent determination of local critical properties $(Re^*_{cr,l}, \alpha_{cr,l}, \beta_{cr,l})$ with $\cot\chi = 0.1, 1, 10$, obtained using (2.7) for $\phi = 30^\circ$, 45°, 60° and 90°. These are then mapped to * parameters defined by (3.3*a–d*), where they are seen to collapse onto the PCP curve in figure 3(*b*). This collapse is expected for all ϕ and χ, which has been further tested numerically for other χ, but not shown here. Since the GCP global critical parameters $Re_{cr}(\theta, \phi)$, $\alpha_{cr}(\theta, \phi)$, $\beta_{cr}(\theta, \phi)$ always correspond to some particular set of local critical parameters, their mapped versions also must lie somewhere on the curve of figure 3(*b*). It follows that all global critical parameters for GCP stability must lie on this curve.

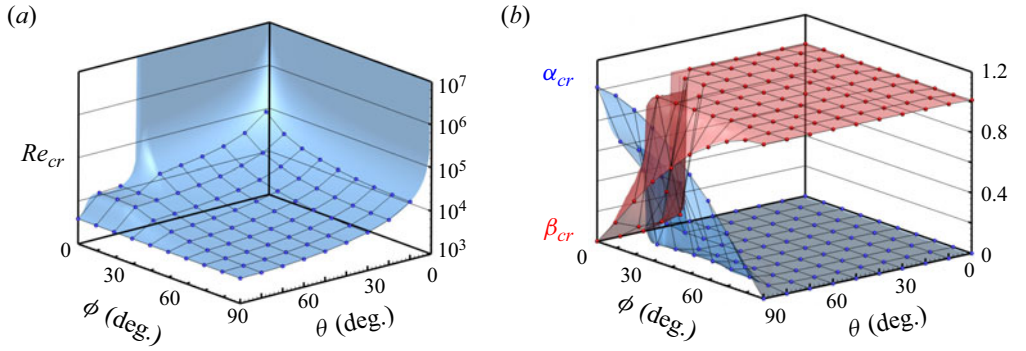

Figure 4. Global critical properties in a 3-D plot: (*a*) global critical Reynolds number Re_{cr}; (*b*) global critical wavenumbers α_{cr} and β_{cr}. Surface composed of data in the ϕ–θ plane with intervals of 0.1°. Dots for data with intervals of 10° show the general behaviour.

3.2. *Calculation of critical parameters*

The above mapping further indicates a method for determination of global critical states for GCP flow. Starting with (3.2), a neutral surface $f^*(\theta^*; Re^*, \alpha, \beta) = 0$ can be determined. In (Re^*, α, β) space, there is a different neutral surface for each θ^*. For given $(\theta, \phi; \alpha, \beta)$, θ^* can be calculated from (3.3*a–d*). Since α, β are specified, Re^* can be calculated. With known Re^*, Re can be calculated from the last of (3.3*a–d*). An algorithm can be summarized as follows.

(i) Specify (θ, ϕ).
(ii) For each (α, β) over some range:
  (*a*) calculate θ^* from the first of (3.3*a–d*),
  (*b*) using (3.2) determine Re^* on the neutral surface $\mathrm{Im}[c^*] = 0$,
  (*c*) calculate the corresponding Re from the last of (3.3*a–d*).
(iii) Over the range of (α, β) chosen, find the minimum Re, which is Re_{cr}. This will also give the corresponding $(\alpha_{cr}, \beta_{cr})$. That is the red point in figure 3(*a*).
(iv) Over the ranges of (θ, ϕ), this will give Re_{cr}, α_{cr} and β_{cr} as functions of (θ, ϕ).

4. Global critical parameters for GCP flow instability

Here we discuss global GCP critical state properties. Figure 4 shows 3-D plots of $Re_{cr}(\theta, \phi)$, $\alpha_{cr}(\theta, \phi)$ and $\beta_{cr}(\theta, \phi)$. Coloured isosurfaces are constructed with data at intervals of 0.1° in both θ and ϕ, with symbols at intervals of 10° overlayed for clarity. As $\theta \to 0^\circ$, for PC flow, $Re_{cr} \to \infty$. As both θ and ϕ increase, Re_{cr} decreases monotonically, displaying $Re_{cr} \to 3848$ at $\theta \to 90^\circ$ for pure PP flow. For PCP flow with $\phi = 0^\circ$, there is singular behaviour with $Re_{cr} \to \infty$ for $\theta < 62.17^\circ$, with finite Re_{cr} for $\theta > 62.17^\circ$. For all $\phi > 0^\circ$, Re_{cr} is finite except in the PC flow limit $\theta = 0^\circ$.

Isosurface plots of corresponding $\alpha_{cr}(\theta, \phi)$ and $\beta_{cr}(\theta, \phi)$ are shown in figure 4(*b*). At $\phi = 0^\circ$ for PCP flow, $\beta_{cr} = 0$ for $\theta > 62.17^\circ$ where Re_{cr} is finite, indicating zero z-direction perturbation. At fixed ϕ when θ decreases from $\theta = 90^\circ$, β_{cr} increases almost discontinuously to near its maximum with a corresponding decrease of α_{cr}. For the region where $\theta \lesssim 60^\circ$, α_{cr} is generally small, and finite β_{cr} dominates critical perturbations. Both maximum values of α_{cr} and β_{cr} are approximately 1.02, the value for PP flow instability (Orszag 1971). Figure 4(*b*) clearly shows a region of the θ–ϕ plane where both α_{cr} and

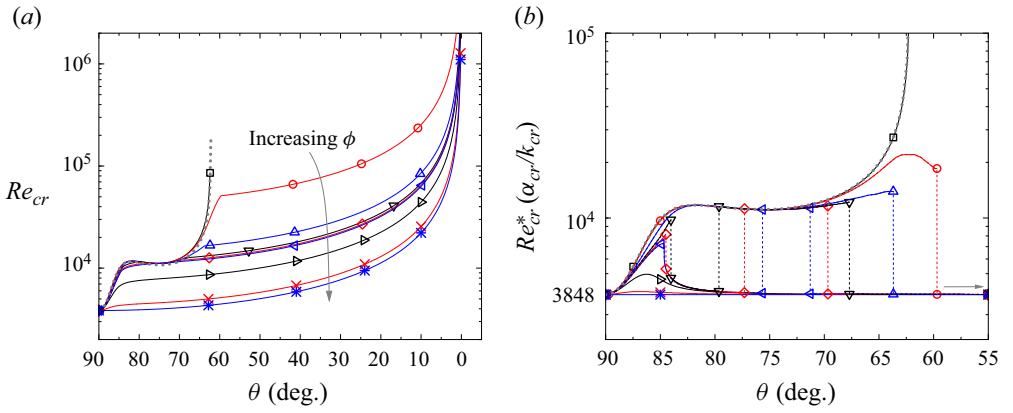

Figure 5. (*a*) Plot of Re_{cr} versus θ for different ϕ. (*b*) Scaling using $Re^*_{cr}(\alpha_{cr}/k_{cr})$ for different ϕ with $Re^* = Re\,(\alpha_1/\alpha)(\sin\theta/\sin\theta^*)$. Dashed lines indicate discontinuities with no data points. For $\theta < 55°$, data collapse on 3848. The dotted line indicates PCP results. Values of ϕ: square, 0°; circle, 5°; up triangle, 15°; down triangle, 19°; diamond, 20°; left triangle, 20.5°; right triangle, 30°; ×, 60°; ∗, 90°.

β_{cr} display rapidly varying, non-monotonic and even discontinuous features. This is now discussed.

4.1. *Scaling of Re_{cr}*

In figure 5(*a*), we show the global Re_{cr} versus θ. Nine cases with different ϕ are shown, which are divided into three groups. The first set includes $\phi = 0°, 5°, 15°$, relevant to discussion of the deviation behaviour from PCP flow stability. The second set considers $\theta = 19°, 20°, 20.5°$, with focus on rapid changes in this medium ϕ region. The third set comprises $\theta = 30°, 60°, 90°$, useful for discussing general trends and possible scaling. The PCP curve ($\phi = 0°$), as noted previously, shows rapidly increasing Re_{cr} when $\theta \to \theta_c \approx 62.17°$. For GCP flow, Re_{cr} deviates substantially from the PCP curve, indicating non-differentiable variation at $\theta \approx 60°$ for $\phi \lesssim 20°$. The subregion where both GCP and PCP results collapse shrinks with increasing ϕ. For $\phi \gtrsim 20°$, Re_{cr} for GCP stability generally diverges from the PCP data trend.

Following our previous hypothesis, the mapped Re^*_{cr} in (3.3*a–d*) is employed using critical wavenumbers α_{cr} and β_{cr}. In order to avoid sparsely scattered values of Re^*_{cr} in the range 10^3 to 10^{20}, we instead plot $Re^*_{cr}\alpha_{cr}/k_{cr}$ versus θ as shown in figure 5(*b*), where the region of $\theta \lesssim 55°$ is not shown owing to the reasonable collapse with $Re^*_{cr} \approx 3848$, corresponding to literature data at $Re_{cr} = 5772$ via the mapping transformation for PCP flow. Two common, interesting tendencies are apparent in figure 5(*b*). One is the sharp decrease of Re_{cr} that takes place over a relatively small θ range; as ϕ increases, there is a monotonic decrease in the value of θ at which this sharp decrease in Re^*_{cr} occurs. The second tendency is the gradual increase of Re^*_{cr} for decreasing θ beginning at $\theta = 90°$. This increase is strongest for PCP flow at $\phi = 0°$, and then weakens with increasing ϕ, with the apparent local maximum occurring at increasing θ. At $\phi \approx 19°$ in the figure, several discontinuities of Re_{cr} are apparent, which can be ascribed to competition between x- and z-direction wavenumbers α and β, respectively.

With further scaling of θ^*, all $Re^*_{cr}\alpha_{cr}/k_{cr}$–$\theta^*$ will collapse onto the PCP results, which is guaranteed for local critical Reynolds numbers with fixed β/α, as demonstrated in figure 3. This collapse of local properties is not useful, however, for identifying behaviour

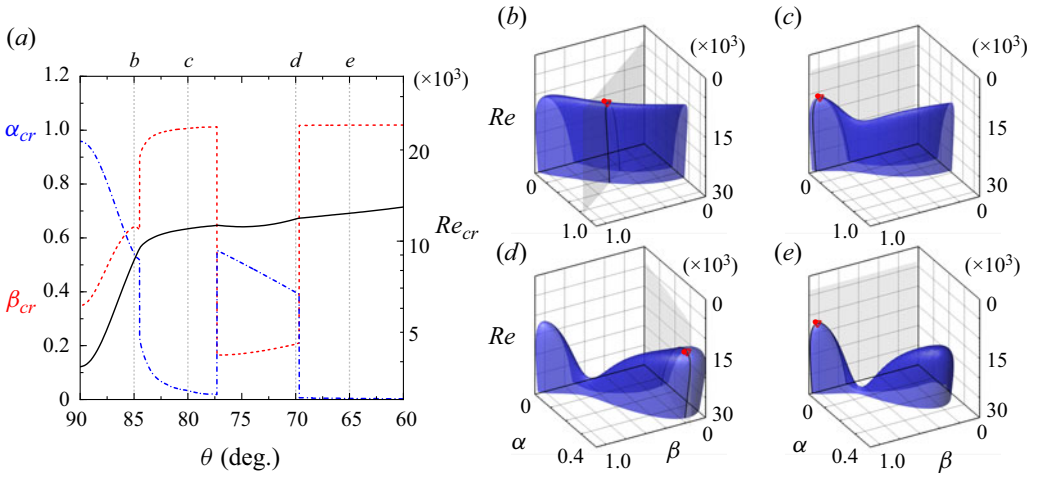

Figure 6. General behaviour of global critical parameters for $\phi = 20°$: (*a*) α_{cr} (dot-dashed line), β_{cr} (dashed line) and Re_{cr} (solid line). Cases at four θ are represented by dotted lines with corresponding data shown in: (*b*), point '*b*', $\theta = 85°$; (*c*), point '*c*', $\theta = 80°$; (*d*), point '*d*', $\theta = 70°$; (*e*), point '*e*', $\theta = 65°$. Blue for the neutral surface, grey plane for $\alpha/\beta = \alpha_{cr}/\beta_{cr}$, intersection line for neutral curve, red dot for corresponding global critical state.

of the global Re_{cr}–θ relationship since the GCP–PCP transformation is heavily distorted in parameter space, with multi-valued subdomains, and thus does not provide a clear one-to-one mapping for global critical parameters.

4.2. *Critical wavenumbers α_{cr} and β_{cr}*

The complex variation of Re^*_{cr} implies an intrinsic competition between α_{cr} and β_{cr}. In figure 6, we focus on the flow with $\phi = 20°$, discussing the competing behaviour of two critical wavenumbers, with neutral surface illustrations at several θ. In figure 6(*a*), we show the α_{cr}, β_{cr} and Re_{cr} variation with θ. It is apparent that Re_{cr} is always continuous but with discontinuous derivatives at certain θ where both α_{cr} and β_{cr} show discontinuities. With decreasing θ, α_{cr} decreases gradually with corresponding increase of β_{cr}. At θ slightly smaller than 85°, α_{cr} drops discontinuously to a smaller value, while β_{cr} also jumps discontinuously. With further decrease of θ to less than 77°, a rebound of α_{cr} and a corresponding fall of β_{cr} can be seen. Further decrease in θ gives a gradual decrease of α_{cr}. At $\theta \lesssim 70°$, another discontinuity appears, with α_{cr} recovering to a small value, while β_{cr} returns to almost its maximum.

To depict these three discontinuities, we provide four neutral surface plots. The first is at $\theta = 85°$ in figure 6(*b*), where the 3-D neutral surface is semi-transparent blue and the grey plane corresponds to the α_{cr}–β_{cr} plane, the global critical state. The intersection of the two surfaces gives the global Reynolds number Re_{cr}. On the neutral surface, the local Reynolds number varies slowly with increasing θ. At the global critical point, $(\alpha_{cr}, \beta_{cr})$ is at a comparable scale, which indicates that the critical stability is determined by contributions from both PCP flow in the x-direction and PP flow in the z-direction.

In the second case, $\theta = 80°$ in figure 6(*c*), the middle region of the neutral surface shifts to higher Reynolds number, and two small Re regions are shown, while Re_{cr} locates on the smaller α_{cr} valley (in the sense of a local minimum Re) or lobe. This is consistent with the first discontinuity noted above. Similarly, in all cases of $\theta \in [77.5°, 84°]$, the

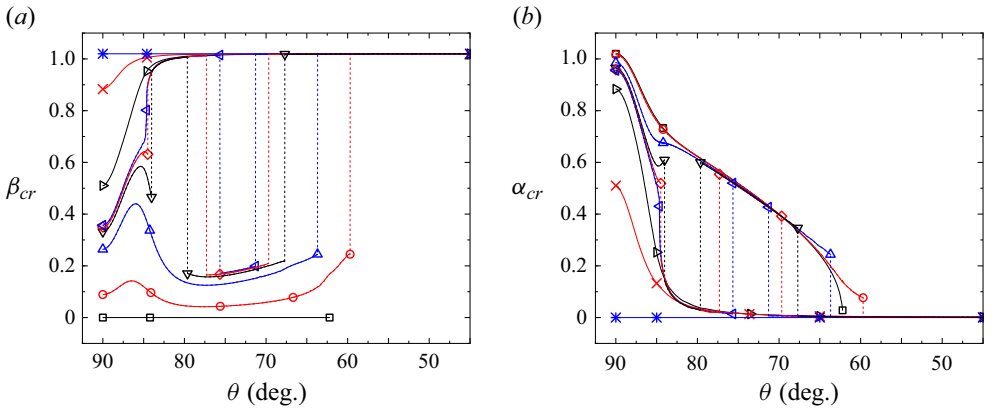

Figure 7. Global critical wavenumbers: (*a*) $\beta_{cr}(\phi, \theta)$, (*b*) $\alpha_{cr}(\phi, \theta)$. Lines with symbols represent different ϕ, referring to figure 5. Vertical dashed lines represent discontinuous jumps that accompany critical state jumps between lobes of the neutral surface.

critical stability is dominated by PP flow in the z-direction. With θ decreasing to 70° in figure 6(*d*), both lobes of the neutral surface contract, while Re_{cr} jumps onto the relatively larger α lobe, producing the second discontinuity in critical wavenumbers. For this case, the dominant part of the flow is PCP flow in the x-direction. The flow with $\theta = 65^\circ$, in figure 6(*e*), shows that Re_{cr} jumps back to the small α lobe, representing the third and final discontinuity with varying θ. Through these rapid changes of flow patterns, the wavenumber α_{cr} remains positive but small. The critical stability is again dominated by z-direction perturbed Poiseuille flow, and this pattern remains as θ further decreases to zero. This interpretation for $\phi = 20^\circ$ clarifies that the discontinuous behaviour of critical wavenumbers is compatible with the idea of wavenumber jumping/competition.

Critical wavenumber behaviour at different ϕ can vary from that discussed above. Variation of β_{cr}–θ is shown in figure 7(*a*), where nine cases are again adopted. Except for $\phi = 0^\circ$, all other flows show non-zero values. For $\phi = 5^\circ$, β_{cr} shows a mild peak around $\theta = 86^\circ$, then maintains a relatively small-value range until a sharp increase to approximately unity at $\theta \approx 60^\circ$. With increasing ϕ, the increase discontinuity in θ moves towards $\theta = 90^\circ$, and the small peak migrates towards lower θ. The case $\phi = 15^\circ$ shows behaviour similar to that for $\phi = 5^\circ$. For $\phi = 19^\circ$, a second peak region is seen, which adds two additional discontinuities. With further increase in ϕ, the first discontinuity at $\theta \approx 84^\circ$ tends to be small, while the other two discontinuities become closer in θ. The two discontinuities disappear quickly with further increase in ϕ. With $\phi = 30^\circ, 60^\circ, 90^\circ$, complex discontinuous behaviour in $\beta_{cr}(\theta, \phi)$ is not observed, and variation with θ is smooth and monotonic.

Figure 7(*b*) shows α_{cr} with corresponding discontinuities. The case $\phi = 5^\circ$ is quite close to $\phi = 0^\circ$ except for $\theta \lesssim 65^\circ$. This shows that for small ϕ, although β_{cr} is not zero for any θ_{cr}, stability is still α_{cr}-dominant, gradually deviating from PCP stability.

5. Conclusion

Analysis of the neutral surfaces/curves and critical state properties of the linear, modal stability of generalized Couette–Poiseuille (GCP) flow has been explored. A GCP flow is generated by the shear provided by the velocity-difference vector of two relatively

moving parallel plates defining an x-direction shear flow and a volume flow produced by an externally applied pressure gradient vector inclined at an angle ϕ to the x-axis. The base flow consists of a superposition of plane Couette (PC) and plane Poiseuille flows that gives a 3-D velocity field where the mean velocity is always parallel to the channel walls but rotates such that both its magnitude and flow angle are functions of the wall-normal coordinate between plates. A parameter set (Re, θ, ϕ) in spherical coordinates, with radius a Reynolds number Re, polar angle θ and azimuthal angle ϕ, defines a particular GCP flow, with $\tan\theta$ describing the relative proportion of Couette-type and Poiseuille-type contributions. Both x-direction (wavenumber α) and z-direction (wavenumber β) perturbations are discussed. The GCP class of flows is unusual in that Squire's theorem does not apply. For the special case of plane Couette–Poiseuille (PCP) flow ($\phi = 0^\circ$), it defines a three parameter $(\theta; Re, \alpha)$ stability problem. The critical coefficients extracted from the present 3-D PCP results agree well with corresponding data of Potter (1966).

Properties of the neutral surface $f(\theta, \phi; Re, \alpha, \beta) = 0$ for GCP flow, defined in (Re, α, β) space for (θ, ϕ) fixed, are discussed. A mapping from GCP to an equivalent PCP stability is found, from which local critical scaling relations θ^* versus $Re^*_{cr,l}\,\alpha_{cr,l}/k_{cr,l}$, where $Re^* = Re\,(\alpha_1/\alpha)\,(\sin\theta/\sin\theta^*)$ and $\tan\theta^* = (\alpha_1/\alpha)\tan\theta$ with $\alpha_1 = \alpha\cos\phi + \beta\sin\phi$, collapse all data for a fixed perturbation wavenumber direction, which is equivalent to a linear relation between local orthogonal scalar wavenumbers. This demonstrates a general failure of Squire's theorem. The global critical Re_{cr} shows continuous variation in (θ, ϕ) space with certain singular limits that includes PC flow, while α_{cr} and β_{cr} have complex behaviour with discontinuities produced by jumps across different lobes of the neutral surface. In particular, the example illustrated with $\phi = 20^\circ$ displays three discontinuities in θ of a type not seen for PCP flow stability. This discontinuous behaviour appears for all $\phi \lesssim 21^\circ$, while for larger values, both $\alpha_{cr}(\theta)$ and $\beta_{cr}(\theta)$ are generally smooth and monotonic.

The present study of GCP flow provides a useful reference for stability analysis of two-dimensional perturbations imposed on a base velocity profile with wall-normal twist. An interesting and open question is whether the GCP $\rightarrow$ PCP mapping described here is applicable to wider classes of 3-D mean velocity profiles, perhaps suggesting further novel, discontinuous neutral surface dynamics with corresponding failure of Squire's theorem and complex critical-property behaviour.

Funding. This work was supported by the National Natural Science Foundation of China (nos 12172352, 12388101), the Strategic Priority Research Program of the Chinese Academy of Sciences (no. XDB0500300) and the National Key R&D Program of China (no. 2022YFA1005200).

Declaration of interests. The authors report no conflict of interest.

Author ORCIDs.
W. Cheng https://orcid.org/0000-0003-3960-4162;
H. Ma https://orcid.org/0009-0008-8465-5990;
D.I. Pullin https://orcid.org/0009-0007-5991-2863;
X. Luo https://orcid.org/0000-0002-4303-8290.

References

Bergström, L.B. 2005 Nonmodal growth of three-dimensional disturbances on plane Couette–Poiseuille flows. *Phys. Fluids* **17** (1), 014105.

Böberg, L. & Brösa, U. 1988 Onset of turbulence in a pipe. *Z. Naturforsch.* **43** (8–9), 697–726.

BUTLER, K.M. & FARRELL, B.F. 1992 Three-dimensional optimal perturbations in viscous shear flow. *Phys. Fluids* **4** (8), 1637–1650.

CHENG, W., PULLIN, D.I., SAMTANEY, R. & LUO, X. 2023 Numerical simulation of turbulent, plane parallel Couette–Poiseuille flow. *J. Fluid Mech.* **955**, A4.

COWLEY, S.J. & SMITH, F.T. 1985 On the stability of Poiseuille–Couette flow: a bifurcation from infinity. *J. Fluid Mech.* **156**, 83–100.

DEARDORFF, J.W. 1963 On the stability of viscous plane Couette flow. *J. Fluid Mech.* **15** (4), 623–630.

GALLAGHER, A.P. & MERCER, A.M. 1962 On the behaviour of small disturbances in plane Couette flow. *J. Fluid Mech.* **13** (1), 91–100.

GITTLER, P. 1993 Stability of axial Poiseuille–Couette flow between concentric cylinders. *Acta Mechanica* **101**, 1–13.

GUHA, A. & FRIGAARD, I.A. 2010 On the stability of plane Couette–Poiseuille flow with uniform crossflow. *J. Fluid Mech.* **656**, 417–447.

HAINS, F.D. 1967 Stability of plane Couette–Poiseuille flow. *Phys. Fluids* **10** (9), 2079–2080.

KIRTHY, S.K. & DIWAN, S.S. 2021 Energy budget analysis and neutral curve characteristics for the linear instability of Couette–Poiseuille flow. *Phys. Fluids* **33** (3), 034102.

LIN, C.C. 1945 On the stability of two-dimensional parallel flows. *Q. Appl. Maths* **3**, 117–142; 218–234; 277–301.

NOUAR, C., KABOUYA, N., DUSEK, J. & MAMOU, M. 2007 Modal and non-modal linear stability of the plane Bingham–Poiseuille flow. *J. Fluid Mech.* **577**, 211–239.

ORSZAG, S.A. 1971 Accurate solution of the Orr–Sommerfeld stability equation. *J. Fluid Mech.* **50** (4), 689–703.

PAL, S. & SAMANTA, A. 2023 Role of slip in the stability of viscoelastic liquid flow through a channel. *Eur. J. Mech.* B **101**, 118–130.

POTTER, M.C. 1966 Stability of plane Couette–Poiseuille flow. *J. Fluid Mech.* **24** (3), 609–619.

REDDY, S.C. & HENNINGSON, D.S. 1993 Energy growth in viscous channel flows. *J. Fluid Mech.* **252**, 209–238.

REN, J., FU, S. & PECNIK, R. 2019 Linear instability of Poiseuille flows with highly non-ideal fluids. *J. Fluid Mech.* **859**, 89–125.

ROMANOV, V.A. 1973 Stability of plane-parallel Couette flow. *Funct. Anal. Applics.* **7** (2), 137–146.

SADEGHI, V.M. & HIGGINS, B.G. 1991 Stability of sliding Couette–Poiseuille flow in an annulus subject to axisymmetric and asymmetric disturbances. *Phys. Fluids* **3** (9), 2092–2104.

SCHMID, P.J. 2007 Nonmodal stability theory. *Annu. Rev. Fluid Mech.* **39**, 129–162.

SENGUPTA, S. & DE, S. 2020 Effect of Couette component on the stability of Poiseuille flow of a Bingham fluid-porous system: modal and non-modal approaches. *Phys. Fluids* **32** (6), 064103.

SHANKAR, B.M. & SHIVAKUMARA, I.S. 2021 Benchmark solution for the stability of plane Couette flow with net throughflow. *Sci. Rep.* **11** (1), 10901.

SMITH, F.T. 1979 Instability of flow through pipes of general cross-section, part 1. *Mathematika* **26** (2), 187–210.

SQUIRE, H.B. 1933 On the stability for three-dimensional disturbances of viscous fluid flow between parallel walls. *Proc. R. Soc. Lond.* A **142**, 621–628.